Innovative 5-m-Off-Distance Inductive Power Transfer Systems With Optimally Shaped Dipole Coils

Changbyung Park, *Student Member, IEEE*, Sungwoo Lee, Gyu-Hyeong Cho, *Senior Member, IEEE*, and Chun T. Rim, *Senior Member, IEEE*

***Abstract*—5-m-off-distance inductive power transfer systems that have optimally shaped cores in the primary and secondary coils are proposed. Instead of conventional-loop-type coils for magnetic resonance scheme, magnetic dipole type coils with cores are used for drastic reduction in deployment space and quite long wireless power transfer. An optimized stepped core structure is also proposed, where a strong magnetic field section is so thick that magnetic field density may be even. Thus, the proposed optimized stepped core has only 41% core loss compared with an unoptimized even core but delivers 2.1 times more wireless power for a given amount of core. Experimentally obtained maximum output powers and primary-coil-to-load-power efficiencies for 3, 4, and 5 m at 20 kHz were 1403, 471, 209 W, and 29%, 16%, 8%, respectively.**

***Index Terms*—Inductive coupling, inductive power transfer system (IPTS), wireless power.**

I. Introduction

EXTENDING the distance of wireless power has a long history beginning with Nikola Tesla trying to make an electric power grid without wires [1]. In 2007, a wireless power transfer scheme using strongly coupled magnetic resonance systems (CMRS) was introduced whose power transfer level and coil-to-coil efficiency are 60 W and 45%, respectively, at a distance of 2 m [2]. CMRS adopted large self-resonant coils at each primary and secondary side to induce a large magnetic field to obtain an extended transfer range. For the high current in these self-resonant coils, the internal resistances of the coils must be very small. This means that the coils must have very high Q factors, which consequently result in very thick wires. The high Q factors also result in substantial voltage stresses on the coils because the coils should sustain Q times larger reactive current or voltage than the corresponding current or voltage of the real power. For example, 1 MVA rating of coil is required to deliver 400 W for $Q = 2500$. To sustain high voltage stress among wires in the coil, the coils cannot help being bulky with large air gap between adjacent wires. Furthermore, the resonant frequencies of the coils are not set by lumped capacitors and inductors but by their inherent stray capacitances and inductances. The stray capacitances and inductances are too sensitive to surroundings such as temperature, humidity, and human proximity [3], [4]. With high Q factors that result in extremely narrow resonant frequency bandwidth and moving resonant frequency due to environmental sensitivity, a complicated automated matching system is needed to track and tune up the resonant condition of the high Q coils using switched inductors and capacitors [5], [6]. Even though a tuning up scheme is applied, matching the multiple resonant coils with high environmental sensitivity is extremely difficult in practice. Due to the distributed coil structure of parasitic capacitance and inductance, the operating frequency of the CMRS tends to be of the order of 10 MHz, which results in the use of RF power amplifiers rather than efficient switching converters [6]. The CMRS for 60-W power transferred over the distance of 50 cm has an apparently high coil-to-coil efficiency of 80% [7]; however, its system efficiency including power source and ac–dc conversion would be quite low. These characteristics are why the well-known CMRS is seldom used in high-power applications. Therefore, inductive power transfer systems (IPTS) have been widely used [8]–[35] for applications that consume more than tens of watt.

In this paper, an IPTS driven by an inverter of 20-kHz switching frequency for 5-m-off distance is proposed. Magnetic dipole coils of narrow and long structure, having ferrite cores inside, are adopted for the primary and secondary coils, minimizing parasitic effects [35]. Optimum-stepped core structures that minimize core loss for a given amount of ferrite material are newly proposed. It is verified by simulations, analyses, and experiments for 20 and 105 kHz that the IPTS, which has been, so far, believed to be adequate for proximity wireless power transfer only, is quite suitable for long distance power delivery as well.

Manuscript received October 21, 2013; revised January 5, 2014; accepted February 22, 2014. Date of publication March 11, 2014; date of current version October 7, 2014. This paper was presented in part at the ECCE-ASIA 2012. This work was supported by the National Research Foundation of Korea Grant funded by the Korea government (MEST) under Grant 2010-0029179, and also by the Nuclear Power Core Technology Development Program of KETEP, granted financial resource from the Ministry of Trade, Industry, and Energy, Republic of Korea (20121610100030). Recommended for publication by Associate Editor U. K. Madawala.

C. Park and G.-H. Cho are with the Department of Electrical Engineering, Korea Advanced Institute of Science and Technology, Daejeon 305-755, Korea (e-mail: pcb@kaist.ac.kr; ghcho@ee.kaist.ac.kr).

S. Lee is with Samsung Electronics, Yong-in 446-711, Korea (e-mail: leesungwoo@kaist.ac.kr).

C. T. Rim is with the Department of Nuclear and Quantum Engineering, Korea Advanced Institute of Technology, Daejeon 305-755, Korea (e-mail: ctrim@kaist.ac.kr).

Color versions of one or more of the figures in this paper are available online at http://ieeexplore.ieee.org.

Digital Object Identifier 10.1109/TPEL.2014.2310232

II. Primary and Secondary Coil Design

A. Overall Coil Configuration

The overall configuration of the IPTS, which is composed of an inverter, capacitor banks, a rectifier, and load as well as

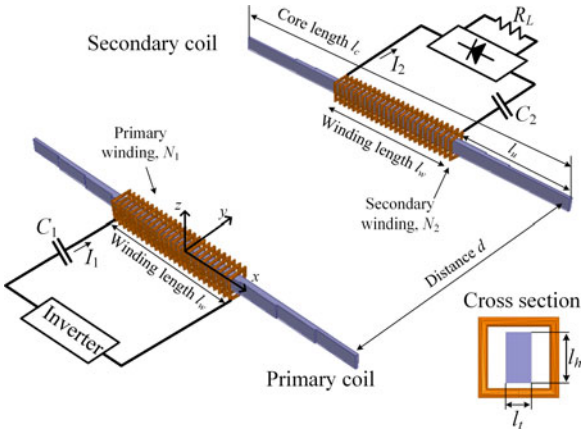

Fig. 1. Overall configuration of the proposed IPTS including primary and secondary coils.

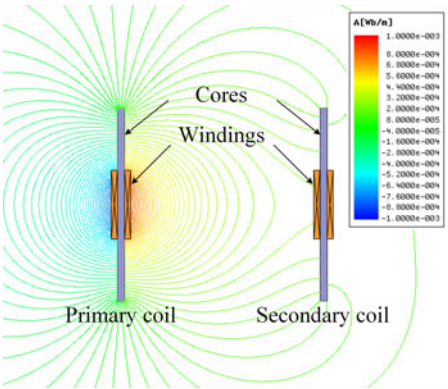

Fig. 2. Simulation result of the magnetic flux lines of the proposed coil configuration, where $d = 3$ m, $I_1 = 10$ A.

proposed primary and secondary coils, is shown in Fig. 1. The primary and secondary windings are wound around the center of primary and secondary cores, and its winding shape is analogous to a helical coil. Each winding is composed of a litz wire to reduce the ac series resistance of the coils. The current of the primary winding generates magnetic field, and then the linkage magnetic flux induces the voltage at the secondary winding.

If an air coil were used, the inner part of the coil would have large magnetic reluctance whereas the outer part of it would have relatively very small magnetic reluctance because of the large effective field crossing area of the outer part of the coil. Strong magnetic field generation, which is crucial for longer distance power delivery, is limited by the large magnetic reluctance of the inner part of the air coil. To reduce this magnetic reluctance, a long rod-type ferrite core is inserted into the air coil, as shown in Fig. 1. As a rule of thumb, this ferrite coil generates about 50 times stronger magnetic field intensity than the air coil by means of the magnetic reluctance reduction.

Magnetic flux lines between the primary and secondary coils are shown in Fig. 2, representing that parts of magnetic flux lines are effectively interlinked to the secondary coil. To make a larger linkage flux, a longer ferrite rod should be inserted. The simulations, throughout this paper, were performed by Ansoft Maxwell v14.0.

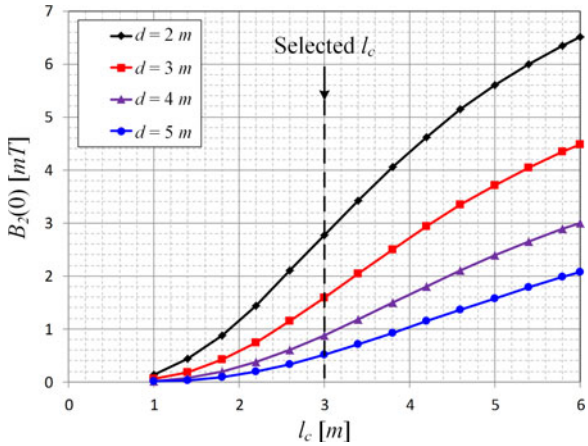

Fig. 3. Simulation results of the magnetic flux density at the center of the secondary coil for the primary and secondary core length l_c (1–6 m) and various distances d (2–5 m). $l_c = 3$ m was selected as the baseline design in this paper.

The rms value of the induced voltage of the secondary coil V_2 is proportional to the rms value of the magnetic flux crossing its winding $B_2(x)$ as follows:

$$V_2 = \omega \overline{B_2(x)} A_2 N_2 \tag{1}$$

where the winding is evenly distributed, ω is the angular switching frequency, A_2 is the cross-sectional area of the secondary coil near center $l_{h2} \cdot l_{t2}$, N_2 is the number of turns of the secondary coil, and the averaged magnetic flux density over the winding length l_w is determined as follows:

$$\overline{B_2(x)} \equiv \frac{1}{l_w} \int_{-l_w/2}^{l_w/2} B_2(x) dx. \tag{2}$$

The simulated magnetic flux density at the center of the secondary coil $B_2(0)$ versus the primary and secondary core length l_c for various distances d is shown in Fig. 3, where the core lengths of the primary and secondary cores are assumed to be same. The longer core length is, the larger magnetic flux density in the secondary core is. For a longer distance of power transfer, the core should be lengthened. As shown in Fig. 3, the core length of 1–2 m is too short for 5-m-off power transfer because of the very low magnetic flux density; however, it becomes considerably increased if the core length is 3 m.

Concerning the winding length l_w, the magnetic linkage flux passing through the secondary winding increases as l_w decreases, as shown in Fig. 2; hence, $l_w = 0$ is the optimum condition for maximizing the induced voltage, as was identified from (2) as follows:

$$\begin{aligned} \mathrm{Max}\left\{\overline{\mathrm{B_2(x)}}\right\} &= \lim_{l_w \to 0} \frac{1}{l_w} \int_{-l_w/2}^{l_w/2} B_2(x) dx = B_2(0) \\ &= \mathrm{Max}\left\{\mathrm{B_2(x)}\right\}. \end{aligned} \tag{3}$$

In practice, (3) cannot be realized because the narrowed winding length deteriorates the frequency response due to parasitic capacitances between each coil winding and between core and winding, respectively, as shown in Fig. 9. Furthermore, local

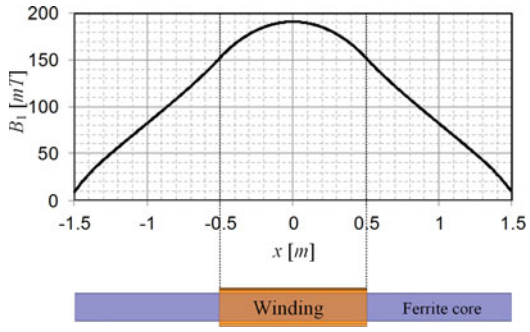

Fig. 4. Simulated magnetic flux density for the primary coil with even thickness of ferrite core $l_{t1} = 7$ *cm*, when $l_c = 3$ m and $l_w = 1$ m. The number of turns is 22 and the primary current I_1 is 40 $A_{\rm rms}$ to reach the saturation level of 190 mT.

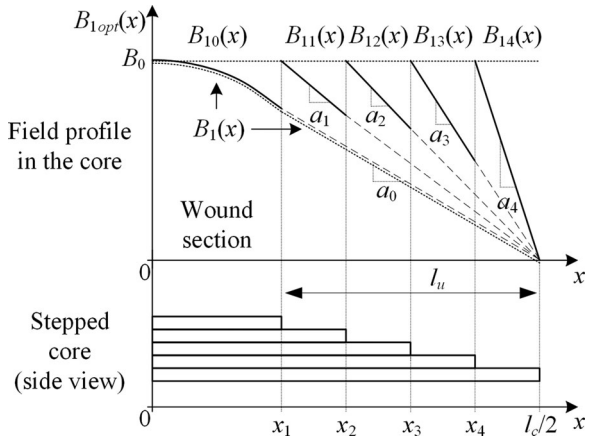

Fig. 5. Magnetic flux density profile of the proposed stepped core. x_1, x_2, x_3, and x_4 denote the junctions of each stepped core.

core saturation may occur for a large secondary current due to concentrated magnetic flux if l_w is too small.

B. Optimized Design of the Proposed Stepped Core

Conventional ferrite material has a saturation flux density of about 300 mT at room temperature, but practically, the maximum should be less than 200 mT considering the core loss and temperature increase of the material due to the loss. The higher temperature of the ferrite material decreases the saturation flux density. If the thickness of the ferrite core along the x-axis is even, the magnetic flux density profile in the ferrite core is not uniform along the longitudinal line (x-axis), as shown in Fig. 4. This uneven profile can be easily anticipated from Fig. 2, where the magnetic linkage of each side is concentrated at the center of the core; hence, the magnetic flux density becomes highestat the center of the core and gradually decreases for the outer section. Therefore, the lower magnetic field section of other parts does not have to be thick. Even though applicable to the secondary coil, this optimum core design, in this paper, is focused on the primary coil, which undergoes severe core saturation for generating high magnetic flux.

As shown in Fig. 4, the ampere-turn of the primary coil is found to be 880 [Amp turn] by simulation with the configuration of $l_{h1} = 20$ cm and $l_{t1} = 7$ cm, i.e., $A_1 = 140$ cm^2 to reach

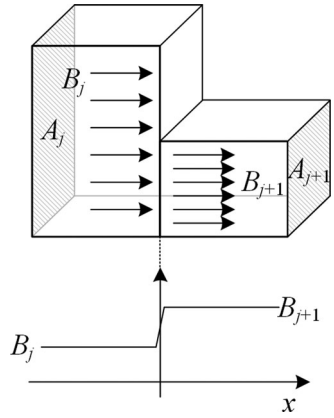

Fig. 6. Magnetic flux distribution at the stepped junction of the ferrite core. Magnetic flux density change is plotted at the bottom.

the magnetic saturation level of 190 mT. Now, the current level of the primary coil I_1 was chosen as 40 $A_{\rm rms}$, considering the current rating of an available inverter; however, it could be so far as the ampere-turn is met. Then, the number of turns of the primary coil N_1 was determined as 22.

The ferrite core thickness should be optimized considering the magnetic field profile. If the total amount of the ferrite material is given, the outer section needs to be thinner so that the magnetic flux density can be uniform. A simple optimum design rule for uniform magnetic flux density is to make the core cross-sectional area as follows:

$$A_{1\rm opt}(x) = \frac{A_1(0)}{B_1(0)} B_1(x) \tag{4}$$

where $A_1(0)$ and $B_1(x)$ are the cross-sectional area and magnetic flux density, respectively, of the even thickness core, as shown in Fig. 6. Under the condition of (4), the magnetic flux density of the proposed optimized core becomes the following:

$$B_{1\rm opt}(x) = \frac{B_1(x)A_1(0)}{A_{1\rm opt}(x)} = \frac{B_1(0)}{A_1(0)} \equiv \frac{B_0}{A_1(0)} = \text{constant}. \tag{5}$$

In other words, if the cross-sectional area is of the same form of magnetic flux density profile of the even thickness core, then uniform magnetic flux density can be obtained.

For fabrication purposes, however, the core length should be finitely segmented, as shown in Fig. 5, where half of the core is presented due to symmetry of the coil. This stepped shape configuration can be easily implemented by small-size ferrite blocks, where the thickness of a block is now 2 cm. It has been assumed that the magnetic flux density profile $B_1(x)$ is unchanged even though $A_{1\rm opt}(x)$ is changed, which shall be valid for the case of this paper where the core thickness is much less than the core length.

The optimization can be done by finding the longitudinal (x-axis) points x_1, x_2, x_3, and x_4, where the magnetic flux density at each stepped junction reaches the maximum value B_0. In this paper, five segmentations were assumed.

Different from conventional air coils, the exact calculation of the magnetic flux density in the proposed ferrite-core coil is hardly possible, and measuring the magnetic flux density in the

ferrite core is impossible. In this paper, the simulated magnetic flux density profile, as shown in Fig. 4, is numerically modeled, considering the curved and straight line portions, as follows:

$$B_1(x) = \begin{cases} B_w(x) = B_0\{1 - c_0|x|^n\}, \quad \text{for} \\ \qquad |x| < l_w/2 \text{ wound section} & \text{(6a)} \\ B_u(x) = a_0(|x| - x_1) + b_0, \quad \text{for} \\ \qquad l_w/2 < |x| < l_c/2 \text{ unwound section} & \text{(6b)} \end{cases}$$

where $x_1 \approx l_w/2$ and the coefficients are determined from Fig. 5 as follows:

$$a_0 = -\frac{B_w(x_1)}{l_c/2 - x_1},\ b_0 = B_w(x_1) \tag{7a}$$

$$c_0 = 0.9, \quad n = 2.0. \tag{7b}$$

In (7b), the c_0 and n are obtained by curve fitting from Fig. 5.

Similar with (5), an optimized magnetic flux density profile for the stepped core can also be found by approximating the profile to the even magnetic flux density $B_1(0)$. The optimized magnetic flux density profile function is then as follows:

$$B_{1\text{opt}}(x) = B_{10}(x) + B_{11}(x) + B_{12}(x) + B_{13}(x) + B_{14}(x) \tag{8}$$

where

$$B_{10}(x) = B_w(x), \text{for } 0 \le |x| < x_1 \tag{9a}$$

$$B_{11}(x) = a_1(|x| - x_1) + b_1, \ \text{for } x_1 \le |x| < x_2 \tag{9b}$$

$$B_{12}(x) = a_2(|x| - x_2) + b_2, \ \text{for } x_2 \le |x| < x_3 \tag{9c}$$

$$B_{13}(x) = a_3(|x| - x_3) + b_3, \ \text{for } x_3 \le |x| < x_4 \tag{9d}$$

$$B_{14}(x) = a_4(|x| - x_4) + b_4, \ \text{for } x_4 \le |x| < l_c/2. \tag{9e}$$

In (9), what should be determined are 12 constants, i.e., a_i's, b_i's, and x_i's.

First, b_i's are easily found, considering the fact that the initial value of each $B_1i(x_i)$ should be the same as B_0, as shown in Fig. 5. From (9b)–(9e), $B_1i(x_i)$ is found as follows:

$$B_{1i}(x_i) = a_i(|x_i| - x_i) + b_i = b_i = B_0, \quad \text{for } i = 1,\ 2,\ 3,\ 4\,. \tag{10}$$

The magnetic flux should be continuous at the stepped junction of the core, as shown in Fig. 6. The adjacent magnetic flux density B_{j+1} can be found as follows:

$$B_{j+1} = \frac{A_j}{A_{j+1}}B_j\ , \qquad \because\ \phi_{j+1} = A_{j+1}B_{j+1} = \phi_j = A_jB_j. \tag{11}$$

At $x = x_1$, the number of core stacks is changed from five to four; therefore, the magnetic flux density is increased by this ratio of cross-sectional area $A_{10}/A_{11} = 5/4$, as identified from (11). Moreover, the magnetic field density of $B_{11}(x_1)$ should be the same as the maximum allowable magnetic field density B_0, as follows:

$$B_{11}(x_1) = B_0 = \frac{A_{10}}{A_{11}}B_{10}(x_1) = \frac{5}{4}B_{10}(x_1). \tag{12}$$

From (12), x_1 can be calculated by using (6a) and (9a) as follows:

$$x_1 = \frac{1}{(5c_0)^{1/n}}. \tag{13}$$

From (13), x_1 is calculated from (7b) as 0.49 m.

It is noteworthy that the magnetic flux density at the ends of the ferrite core, i.e., $|x| = l_c/2$, is nearly zero, as shown in Figs. 4 and 5. This means that each $B_1i(x)$ has the same zero value at $|x| = l_c/2$, as shown in Fig. 5, because each segmented stacked core assumes even thickness to the ends, i.e.,

$$B_{1i}(l_c/2) = a_i(|l_c/2| - x_i) + B_0 = 0 \ \text{ for i} = 1,\ 2,\ 3,\ 4. \tag{14}$$

From (14), a_i's can be determined as follows:

$$a_i = \frac{-B_0}{l_c/2 - x_i} \text{for } i = 1,\ 2,\ 3,\ 4. \tag{15}$$

Applying (7a) and (12) to (15), a_1 can be determined as follows:

$$a_1 = \frac{-B_0}{l_c/2 - x_1} = -\frac{5}{4}\frac{B_{10}(x_1)}{l_c/2 - x_1} = \frac{5}{4}a_0. \tag{16}$$

Now the coefficients of (9b) are completely determined, and at $x = x_2$, the number of core stacks is changed from four to three; therefore, the magnetic flux density is increased by $A_{11}/A_{12} = 4/3$. Similar with (12), the magnetic field density of $B_{12}(x_2)$ should be the same as the maximum allowable magnetic field density B_0, as identified from (11), as follows:

$$B_{12}(x_2) = B_0 = \frac{A_{11}}{A_{12}}B_{11}(x_2) = \frac{4}{3}B_{11}(x_2)$$

$$= \frac{4}{3}\{a_1(x_2 - x_1) + B_0\}. \tag{17}$$

From (17), x_2 can be determined from the following:

$$x_2 = x_1 + \frac{-B_0}{4a_1} = x_1 + \frac{1}{4}(l_c/2 - x_1) \equiv x_1 + \frac{l_u}{4}. \tag{18}$$

In (18), it was found that the second segmented position corresponds to a fourth of the unwound core length l_u.

By recursive applications of this procedure of finding a_i's and x_i's, as shown in (12)–(18), a complete determination of the coefficients becomes as follows:

$$a_2 = \frac{5}{3}a_0 \tag{19a}$$

$$a_3 = \frac{5}{2}a_0 \tag{19b}$$

$$a_4 = \frac{5}{1}a_0 \tag{19c}$$

$$x_3 = x_2 + \frac{l_u}{4} \tag{20a}$$

$$x_4 = x_3 + \frac{l_u}{4}. \tag{20b}$$

In general, the coefficients for an arbitrary m-segmentation are found to be, so far as the magnetic flux density of the

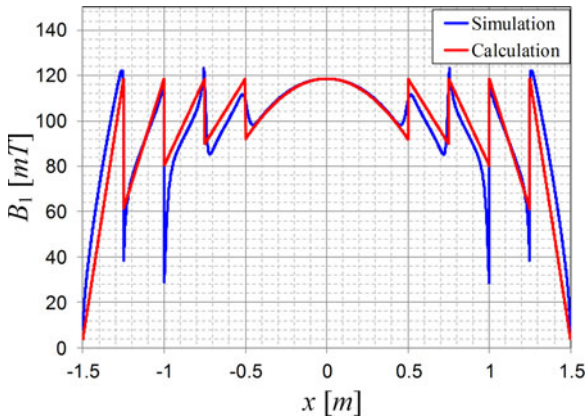

Fig. 7. Comparison of the simulated magnetic flux density profile with the calculated one for the proposed stepped core, when $l_c = 3$ m and $l_w = 1$ m. The number of turns is 22, and the primary current I_1 is 40 $A_{\rm rms}$.

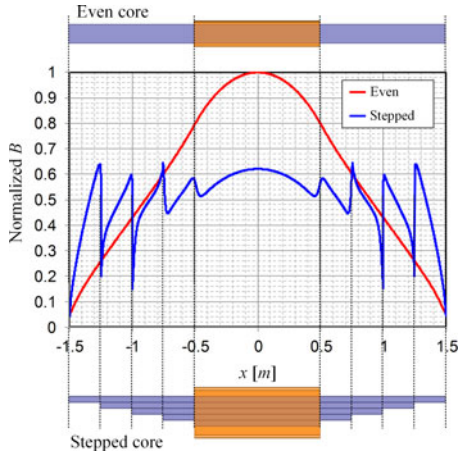

Fig. 8. Simulation results of the normalized magnetic flux density for the stepped core and even core, where $l_c = 3$ m and $l_w = 1$ m. The number of turns is 22, and the primary current I_1 is 40 $A_{\rm rms}$.

unwound core area is of a straight line like in Fig. 4, as follows:

$$a_i = \frac{m}{m-i}a_0 \text{ for } i = 1,\ 2, \ldots,\ m-1 \quad (21a)$$

$$b_i = B_0 \text{ for } i = 1,\ 2, \ldots,\ m-1 \quad (21b)$$

$$x_{i+1} - x_i = \frac{l_u}{m-1} \text{ for } i = 1,\ 2, \ldots,\ m-1. \quad (21c)$$

Using the designed parameters, the calculated magnetic flux density of (8) and the simulated one were compared with each other, as shown in Fig. 7. As anticipated, the magnetic flux density has the peak value B_0 at each stepped junction point (x_1, x_2, x_3, x_4).

Fig. 8 shows the simulation results of the normalized magnetic flux densities for the optimized stepped core and even core, respectively. The amount of used ferrite core for each case is assumed to be same, for fair comparison. It is found that the peak magnetic field of the stepped core is reduced to 65% of that of the even core, which means that 35% of the core can be saved by the proposed stepped core design to achieve same magnetic flux density profile.

The magnetic flux in the core is proportional to the inductance of a coil in general for a given current. Hence, the inductance of the stepped core and even core, $L_{1\rm opt}$ and L_1, respectively, are calculated by simulations for comparison, which are 942 and 991 μH, respectively. Because the inductance of the proposed stepped core is only 4.9% less than the even core, the induced voltage drop is not so significant. Therefore, it can be concluded that the proposed scheme can deliver 2.13 ($=1.46^2$) times wireless power than the even core type for same amount of core, considering the delivered wireless power is proportional to the square of induced voltage of (1) or magnetic flux density, as follows:

$$\frac{P_{1,\rm opt}}{P_1} = \left(\frac{V_{1,\rm opt}}{V_2}\right)^2 = \left(\frac{L_{1,\rm opt}}{L_1} \cdot \frac{B_{0,\rm opt}}{B_0}\right)^2. \quad (22)$$

C. Core Loss Calculation

The magnetic flux is significantly intensified and the coil size becomes quite compact by using the core; however, the penalty of using the core is core loss. As identified from the side view of the proposed stepped core, as shown in Fig. 8, both the total volume and maximum magnetic flux density of a core should be minimized to mitigate the core loss. Hysteresis loss, which is the major source of core loss, can be modeled in watt per unit volume by the following Steinmetz equation [30]:

$$P_{cv} = C_m C_T f^p B_{\rm peak}^q \ [W/m^3],\ C_T = C_{T0} - C_{T1}T + C_{T2}T^2 \quad (23)$$

where C_m and C_T are core loss coefficient and temperature correction parameter, respectively.

Quantitative core loss can be assessed for the even core and optimized stepped core when the amount of core is given. Applying (8) to (23), the ferrite core loss can be analytically calculated as follows:

$$P_{1h} = \iiint P_{cv}\,dxdydz = \int C_m C_T f^p B_{\rm peak}^q A_1(x)dx$$
$$= \begin{cases} C_m C_T f^p \int B_1^q(x) A_1(x)dx, & \text{for even core} \\ C_m C_T f^p \int B_{1\ \rm opt}^q(x) A_{1\rm opt}(x)dx, & \text{for stepped core} \end{cases} \quad (24)$$

where $A_1(x)$ and $A_{1\rm opt}\ (x)$ are the cross-sectional area of the even core and stepped fore, respectively. Parameters for the power loss density of the ferrite core from the maker are summarized in Table I. From (24), the losses for the even core and stepped core were calculated with the temperature of 100 °C and I_1 of 40 $A_{\rm rms}$ by the mathematical software Maple v16.0, and the losses were calculated to be 1340 and 550 W, respectively. Adopting the proposed optimizing technique, the core loss became just 41% of the unoptimized even core.

D. Winding Methods and Parasitic Capacitances

Compared with air coils, the proposed core wound coils have relatively large inductances of the order of mH; therefore, small parasitic capacitances of the coils may affect the self-resonant frequencies of the coils. Two major parasitic capacitances of the core wound coil are shown in Fig. 9. Different from conventional air coils that have just parasitic capacitances C_w between

TABLE I
FIT PARAMETERS TO CALCULATE THE HYSTERESIS CORE LOSS DENSITY

Parameter	Value
C_m	7.13 x 10^3
p	1.42
q	3.02
C_{T2}	3.65 x 10^{-4}
C_{T1}	6.65 x 10^{-2}
C_{T0}	4.00
T	100 °C

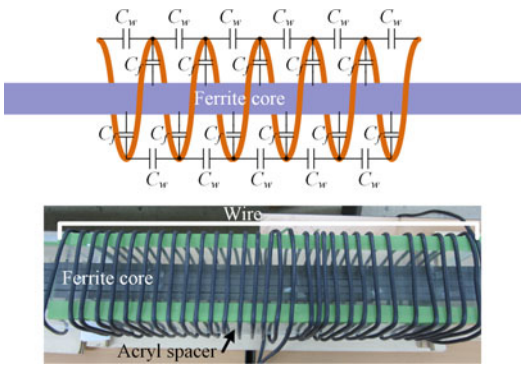

Fig. 9. Parallel parasitic capacitances of ferrite wound coils (upper) and the fabricated coil for minimizing parasitics (lower) for hundred kilohertz operation.

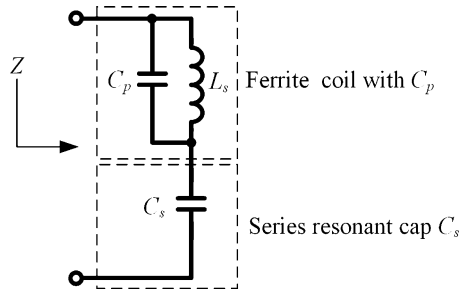

Fig. 10. Resonant tank model comprises of a ferrite wound coil with a parasitic capacitance and a series resonant capacitor.

adjacent wires, the proposed core wound coils have the parasitic capacitances C_f between the wire and core. The C_f of the proposed coil is not negligible because the wire length of the coil is several tens of meters. These parasitic capacitances, C_w and C_f, constitute a parallel capacitance C_p in an equivalent circuit model, as shown in Fig. 10.

Fig. 10 shows the simplified equivalent circuit model of a resonant tank, which is composed of the ferrite wound coils including its parallel parasitic capacitor C_p and a series resonant

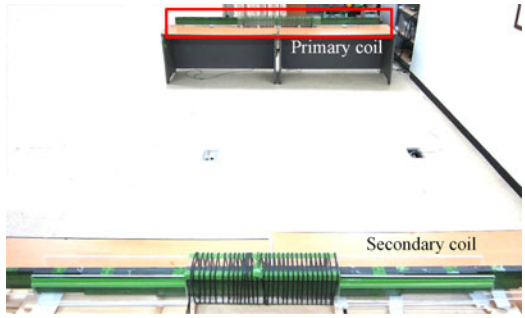

Fig. 11. Picture of the proposed primary and secondary coils with stepped cores and acryl spacers for experiments.

capacitor C_s. Considering that L_s represents either L_1 or L_2, the impedance of the circuit Z is as follows:

$$Z = \frac{1}{j\omega C_s} + \frac{1}{j\omega C_p} || j\omega L_s = \frac{1 - L_s(C_s + C_p)\cdot\omega^2}{j\omega C_s(1 - L_s C_p \omega^2)}$$
$$= \frac{1 - (\omega/\omega_s)^2}{j\omega C_s\{1 - (\omega/\omega_p)^2\}} \quad (25)$$

where the parallel angular resonant frequency ω_p and series angular resonant frequency ω_s are as follows:

$$\omega_p = \frac{1}{\sqrt{L_s C_p}} \quad (26a)$$

$$\omega_s = \frac{1}{\sqrt{L_s(C_p + C_s)}}. \quad (26b)$$

To make the secondary induced voltage large, the number of turns of the secondary winding should be large and the operating frequency should be as high as several hundreds of kilohertz, as identified in (1). To meet these conditions, C_s should be as small as a few nanofarad because of the large L_s of millihertz. As identified from (25), C_p should be at least a few times smaller than C_s in order to separate ω_s far enough from ω_p. To reduce C_f and C_w, an acryl spacer is inserted between the wire and ferrite core, and the wire is wound with a sufficient interwire gap based on the given winding space and the number of turns, as shown in Fig. 9. Thus, the coil can operate over a hundred kilohertz without deteriorating resonance characteristics.

III. EXPERIMENTAL VERIFICATIONS OF THE IPTS

A. Overall Configuration

Experimental verifications of the proposed coils were made in a laboratory, as shown in Fig. 11, where the primary and secondary coils were placed on the tables.

The circuit diagram of the proposed IPTS is shown in Fig. 12, where the primary coil and its series resonant capacitor C_1 are driven by a full bridge inverter. To guarantee zero-voltage switching operation of the inverter, the switching frequency of the inverter was selected to be slightly higher than the primary-side resonant frequency determined by C_1 and L_1 [11]. On the other hand, the secondary-side resonant frequency determined by C_2 and L_2 was tuned exactly to the switching frequency.

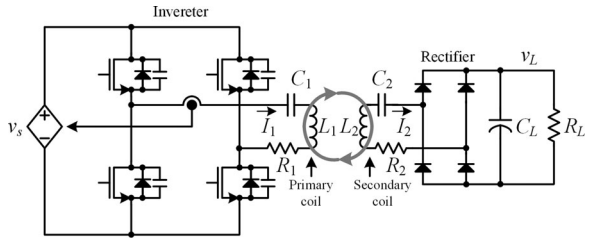

Fig. 12. Circuit diagram of the proposed IPTS for experiments, which includes an inverter for the primary coil driving and a rectifier for the secondary coil.

TABLE II
PARAMETERS OF THE PROPOSED IPTS INCLUDING COILS

Parameters	Values	Parameters	Values
f	20 *kHz*	l_c	3 *m*
d	3 *m* 4 *m* 5 *m*	l_w	1 *m*
L_m	18.5 μH, 10.6 μH, 6.94 μH	x_1	0.5 *m*
κ	0.68% 0.39% 0.26%	x_2	0.75 *m*
L_1	832 μH	x_3	1 *m*
L_2	8.78 *mH*	x_4	1.25 *m*
C_1	80 *nF*	l_{t1}	0.1 *m*
C_2	7.1 *nF*	l_{h1}	0.2 *m*
N_1	22	l_{t2}	0.05 *m*
N_2	86	l_{h2}	0.1 *m*
R_1	0.63 Ω	C_L	220 μF
R_2	4.17 Ω	Q_2	30.2
R_L	40 Ω		

These are summarized as follows:

$$\omega \cong 1.05\,\omega_1 = \frac{1.05}{\sqrt{L_1 C_1}} \tag{27a}$$

$$\omega = \omega_2 = \frac{1}{\sqrt{L_2 C_2}}. \tag{27b}$$

From (27), C_1 and C_2 were determined by using the measured values of L_1 and L_2, which are listed in Table II.

A full bridge rectifier converts the induced ac voltage of the secondary coil to dc voltage. The R_1 and R_2 represent primary and secondary effective series ac resistances, respectively, which include the equivalent series resistances (ESR) of the resonant capacitors and equivalent ac resistances of the coils comprise of conduction loss and eddy current loss. R_L was fixed to 40 Ω throughout the experiments to give 1 kW at 200-V load voltage.

B. Fabrication of Coils

The proposed coils designed in the previous sections were fabricated, as shown in Figs. 9 and 11, which are the stepped core type and even core type. The lengths of primary and secondary cores are all $l_c = 3$ m, and other parameters for fabrication are listed in Table II. For fabrication, we selected a low-priced Mn–Zn type soft ferrite material named PL-7 from Samwha Electronics, Korea because the material's loss characteristic is similar to a Mn–Zn type material called 3C30 produced by Ferrox Cube.

The primary coil inductance L_1 was measured as 832 μH, which is 12% less than the simulated value of 942 μH; this is mainly due to thin isolation films between each ferrite block, which were inserted to mitigate eddy current loss inside the cores.

The acryl spacers were also inserted between the wire and ferrite core to reduce C_f in order to obtain about a 3 cm gap. Thus, the measured parasitic capacitances of the primary and secondary coils, C_{p1} and C_{p2}, were merely 95 and 44 pF, respectively. Comparing these values of C_{p1} and C_{p2} with C_1 = 80 nF and C_2 = 7.1 nF, they are 0.12% and 0.62%, which correspond to 28.9 and 12.7 times frequency separation of (26), respectively. In other words, the parallel resonance frequencies of the primary and secondary coils are 566 and 256 kHz, respectively; hence, the fabricated coils can be used up to about a hundred kilohertz in practice.

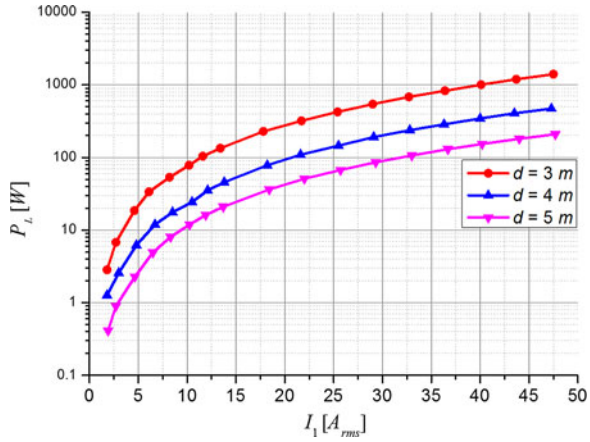

Fig. 13. Measured output power versus the primary rms current I_1 for various distances. (20 kHz).

C. Efficiency Measurements

To measure the power efficiency of the proposed IPTS, the ac input power of the primary coil was measured by a precision digital power analyzer, Yokogawa, WT1800, whereas the dc output power of the load resistor was measured by multimeters. The measured output power versus the primary current I_1 for various distances at 20 kHz is shown in Fig. 13. The maximum output powers for distances 3, 4, and 5 m were 1403, 471, and 209 W at the maximum primary current $I_1 = 47\ A_{\rm rms}$, respectively.

Fig. 14(a) shows the power efficiency measured from the primary coil to the load resistor versus the output power P_L for various distances d. The maximum output powers and efficiencies for 3, 4, and 5 m at 20 kHz were 1403, 471, 209 W, and 29%, 16%, 8%, respectively. The power efficiency decreases as

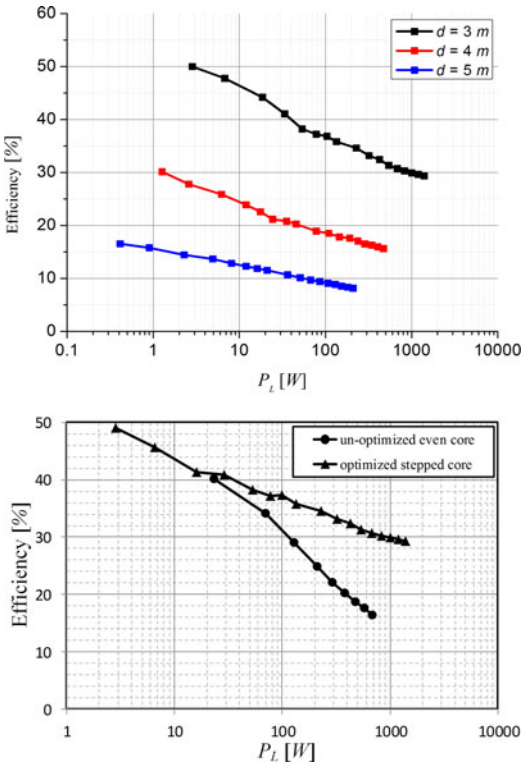

Fig. 14. (a) Measured efficiency from the primary coil to the load resistor versus output power P_L for various distances (20 kHz). (b) Measured efficiency comparison between an unoptimized even core and optimized stepped core, $d = 3$ m.

P_L, or correspondingly, I_1, increases due to the substantially increased hysteresis core losses in the coils. The efficiencies of the unoptimized even core and optimized stepped core are compared in Fig. 14(b). For low load power, the core loss difference between two cases is not substantial because of the undistinguishable core loss difference. As the load power increases, the core loss difference between the optimized case and upoptimized case gets larger because the efficiency of the optimized case is improved due to smaller core loss than unoptimized case.

A much higher operating frequency of 105 kHz was also tried, as shown in Figs. 15 and 16, where a high-priced Mn–Zn type soft ferrite material for higher frequency application up to 1 MHz, named PL-F1 from Samwha Electronics, was used. Now, the input power was measured at the dc input side of the inverter because the power measurements for high frequency with digital power meters incurred numerous errors. As shown in Fig. 15, the maximum output powers for each distance of 2, 3, 4, and 5 m were 109, 34.8, 13.8, and 5.93 W, respectively, where the primary current I_1 was less than 4 $A_{\rm rms}$ due to the power limit of the prototype high-frequency inverter specially made for a hundred kilohertz.

Fig. 16 shows the power efficiency from inverter input to load resistor versus the output power for various distances. For the output power of 5 W, the power efficiencies were 46%, 31%, 15%, and 6% for the distances of 2, 3, 4, and 5 m, respectively. Comparing these results of Fig. 16 with those of Fig. 14, the efficiencies for 105 kHz are apparently lower than that for

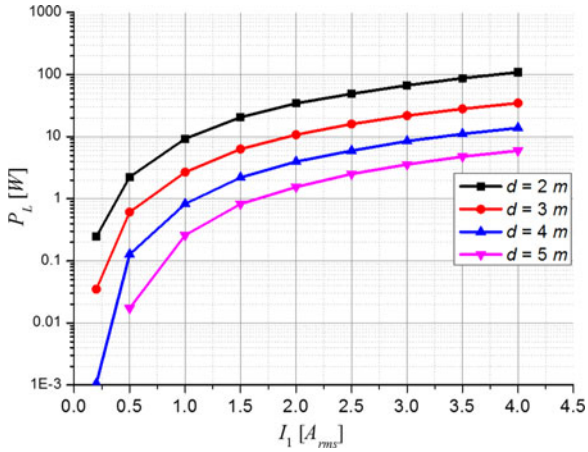

Fig. 15. Measured output power versus primary current I_1 for various distances (105 kHz).

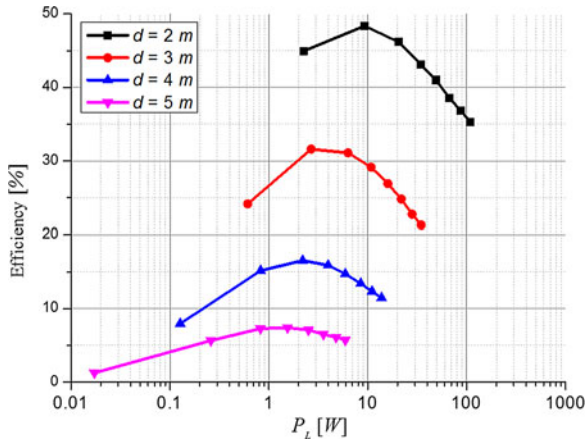

Fig. 16. Measured power efficiency from inverter input to load resistor versus output power P_L for various distances (105 kHz).

20 kHz; however, it is not so obvious because the power measurement method, inverter fabrication, and current level were drastically changed. Higher operating frequency may make the overall system compact; however, it is not straightforward to say that higher operating frequency is optimal in terms of overall power efficiency, output power level, and total cost due to the limited capacitor selection, increased core loss, and parasitic effects.

Detailed studies on the operating frequency selection together with the much longer wireless power delivery by shorter l_c of coils and higher efficiency are left for further work.

D. Loss Measurements

To verify the calculated hysteresis loss in the ferrite core of (24), the loss difference of the primary coils between the optimized stepped core and unoptimized even core, as in (28), was measured:

$$\Delta P_{1h} = C_m C_T f^p \int \{B_1^q(x)A_1(x) - B_{1\rm opt}^q(x)A_{1\rm opt}(x)\}dx. \tag{28}$$

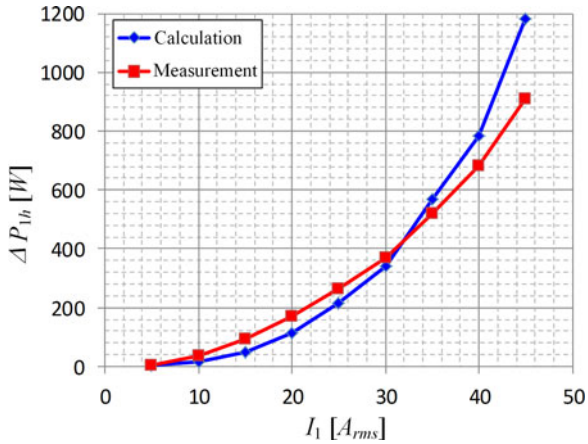

Fig. 17. Measured (red curve) and calculated (blue curve) loss differences of the primary coils between optimized stepped cores and unoptimized even cores at 20 kHz.

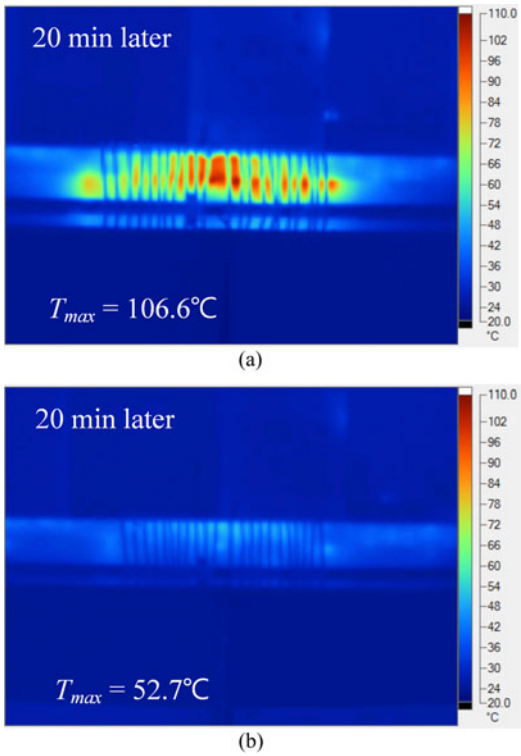

Fig. 18. Measured surface temperature using a thermo-graphic camera after 20 min. Operation of the IPTS at 20 kHz and $I_1 = 40\ A_{\rm rms}$.

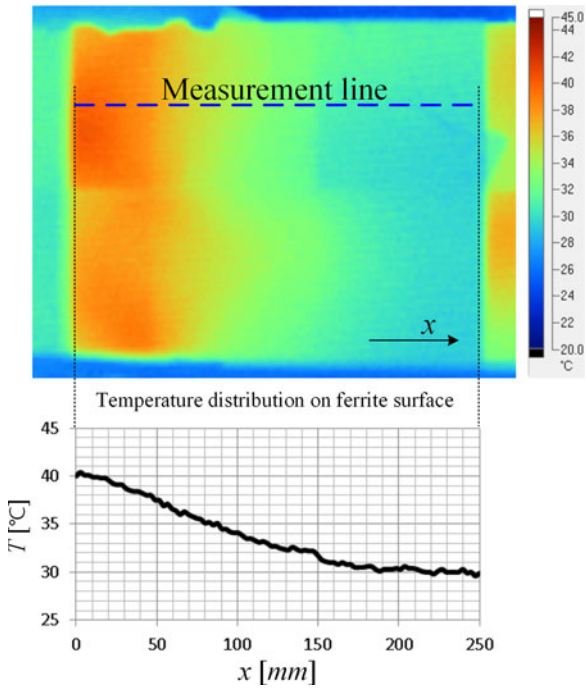

Fig. 19. Measured surface temperature of a segment of the stepped core (side view), showing internal magnetic flux density.

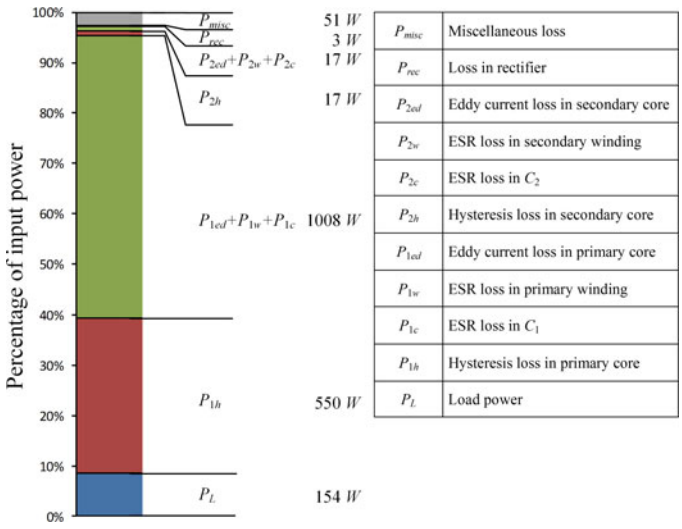

Fig. 20. Example of the power loss analysis of the proposed IPTS with stepped cores at 20 kHz when $d = 5$ m and $I_1 = 40\ A_{\rm rms}$.

Except for the hysteresis losses in the optimized core and unoptimized core, other losses are almost the same. Therefore, other loss components are cancelled out, and only the difference of hysteresis core losses is measured, which is found to be quite similar with (28), as shown in Fig. 17.

The measured surface temperatures of the even core and optimized stepped core for the same amount of ferrite material by using a thermo-graphic camera is shown in Fig. 18. The temperature of the optimized stepped core was much lower than the even core, and the temperature distribution of the optimized stepped core was more uniform than the even core. From this temperature measurement, power loss minimization using the proposed optimization method has been further verified.

The measured surface temperature of a segment of the stepped core is shown in Fig. 19. The surface temperature distribution of core reflects the magnetic flux density profile that cannot be directly measured in a core. The simulated and calculated magnetic flux density profiles, as shown in Fig. 7, correspond well to this measured temperature profile.

Though it is not possible to measure all the detail losses, the loss analysis of the proposed IPTS with stepped cores for an example of the power transfer distance of 5 m and primary current I_1 of 40 $A_{\rm rms}$ at 20 kHz is shown in Fig. 20. Except for the

term P_{misc} which is the remaining unexplained discrepancy, the powers were either measured or calculated; $P_1 h$ and $P_2 h$ were calculated from (24) and all the other powers were measured. The dominant losses are found to be the hysteresis and eddy current losses of the primary coil. Therefore, better a ferrite core should be developed for a long distance wireless power transfer with higher system efficiency.

The parameters of the proposed IPTS are summarized in Table II. The effective ac resistances R_1 and R_2 were measured by tuning the resonant circuits of the primary and secondary coils at the operating frequency of 20 kHz, respectively. The mutual inductance L_m was calculated from the measured induced voltage V_2 for a given primary current I_1. The mutually coupling factor κ was calculated from L_m, L_1, and L_2.

Note that the quality factor of the secondary circuit Q_2 for 20 kHz, considering the effective ac side resistance of dc side resistor [31], is merely 30.2 as follows:

$$Q_2 \equiv \frac{\omega L_2}{R_e} = \frac{\omega L_2}{R_{L,\mathrm{eff}} + R_2} = \frac{\omega L_2}{R_L \frac{8}{\pi^2} + R_2}, \qquad R_{L,\mathrm{eff}} = \left(\frac{2\sqrt{2}}{\pi}\right)^2 R_L. \tag{29}$$

Comparing the very large Q of the CMRS, the proposed Q_2 is about 100 times smaller; hence, the proposed IPTS is well within the practical Q_2 of less than 100, which has been verified by several applications [11], [32], [33].

IV. Conclusion

The 5-m-off-long-distance IPTS has been demonstrated, introducing the possibility of a new remote power delivery mechanism that has never been implemented, even by the CMRS, so far. The dipole structure coil with a ferrite core instead of conventional loop-type coils used in the CMRS is found to be quite effective for a longer power delivery. Its shape is not bulky but narrow and long so that it can be installed in the corner or ceiling of a room. The proposed optimized stepped core has been experimentally verified to have only 41% core loss compared with the unoptimized even core but delivers 2.1 times more wireless power for a given amount of core. Experimentally obtained maximum output powers and primary-coil-to-load-power efficiencies for 3, 4, and 5 m at 20 kHz were 1403, 471, 209 W, and 29%, 16%, 8%, respectively. The proposed IPTS is under development as a potential back-up power of essential sensors during severe accidents in a nuclear power plant.

References

[1] N. Tesla, "Apparatus for transmitting electrical energy," U.S. Patent 1 119 732, Dec. 1, 1914.

[2] A. Kurs, A. Karalis, R. Moffatt, J. D. Joannopoulos, P. Fisher, and M. Soljacic, "Wireless power transfer via strongly coupled magnetic resonances," *Science*, vol. 317, no. 5834, pp. 83–86, Jul. 2007.

[3] L. H. Ford, "The effect of humidity on the calibration of precision air capacitors," *J. Inst. Power Eng.*, vol. 95, no. 48, pp. 709–712, Dec. 1948.

[4] V. J. Brusamarello, Y. B. Blauth, R. Azambuja, I. Muller, and F. R. Sousa, "Power transfer with an inductive link and wireless tuning," *IEEE Trans. Instrum. Meas.*, vol. 62, no. 5, pp. 924–931, May 2013.

[5] T. C. Beh, M. Kato, T. Imura, Sehoon Oh, and Y. Hori, "Automated impedance matching system for robust wireless power transfer via magnetic resonance coupling," *IEEE Trans. Ind. Electron.*, vol. 60, no. 9, pp. 3689–3698, Sep. 2013.

[6] A. P. Sample, D. T. Meyer, and J. R. Smith, "Analysis, experimental results, and range adaptation of magnetically coupled resonators for wireless power transfer," *IEEE Trans. Ind. Electron.*, vol. 58, no. 2, pp. 544–554, Feb. 2010.

[7] Sony Corp. (2009, Oct. 2). Sony develops highly efficient wireless power transfer system based on magnetic resonance. [Online]. Available: http://www.sony.net/SonyInfo/News/Press/200910/09-119E/index.html

[8] J. Hirai, T.-W. Kim, and A. Kawamura, "Study on intelligent battery charging using inductive transmission of power and information," *IEEE Trans. Power Electron.*, vol. 15, no. 2, pp. 335–345, Mar. 2000.

[9] B. L. Cannon, J. F. Hoburg, D. D. Stancil, and S. C. Goldstein, "Magnetic resonant coupling as a potential means for wireless power transfer to multiple small receivers," *IEEE Trans. Power Electron.*, vol. 24, no. 7, pp. 1819–1825, Jul. 2009.

[10] M. Budhia, G. A. Covic, and J. T. Boys, "Design and optimization of circular magnetic structures for lumped inductive power transfer systems," *IEEE Trans. Power Electron.*, vol. 26, no. 11, pp. 3096–3108, Nov. 2011.

[11] J. Huh, S. W. Lee, W. Y. Lee, G. H. Cho, and C. T. Rim, "Narrow-width inductive power transfer system for online electrical vehicles," *IEEE Trans. Power Electron.*, vol. 26, no. 12, pp. 3666–3679, Dec. 2011.

[12] S. H. Lee and R. D. Lorenz, "Development and validation of model for 95%-efficiency 220-W wireless power transfer over a 30-cm Air Gap," *IEEE Trans. Ind. Appl.*, vol. 47, no. 6, pp. 2495–2504, Nov.-Dec. 2011.

[13] H. Matsumoto, Y. Neba, K. Ishizaka, and R. Itoh, "Comparison of characteristics on planar contactless power transfer systems," *IEEE Trans. Power Electron.*, vol. 27, no. 6, pp. 2980–2993, Jun. 2012.

[14] Z. Pantic and S. M. Lukic, "Framework and topology for active tuning of parallel compensated receivers in power transfer systems," *IEEE Trans. Power Electron.*, vol. 27, no. 11, pp. 4503–4513, Nov. 2012.

[15] J. P. C. Smeets, T. T. Overboom, J. W. Jansen, and E. A. Lomonova, "Comparison of position-independent contactless energy transfer systems," *IEEE Trans. Power Electron.*, vol. 28, no. 4, pp. 2059–2067, Apr. 2013.

[16] M. Pinuela, D. C. Yates, S. Lucyszyn, and P. D. Mitcheson, "Maximizing DC-to-load efficiency for inductive power transfer," *IEEE Trans. Power Electron.*, vol. 28, no. 5, pp. 2437–2447, May 2013.

[17] S. Lee, B. Choi, and C. T. Rim, "Dynamics characterization of the inductive power transfer system for online electric vehicles by laplace phasor transform," *IEEE Trans. Power Electron.*, vol. 28, no. 12, pp. 5902–5909, Dec. 2013.

[18] Y. Zhang, Z. Zhao, and K. Chen, "Frequency decrease analysis of resonant wireless power transfer," *IEEE Trans. Power Electron.*, vol. 29, no. 3, pp. 1058–1063, Mar. 2014.

[19] H. Hao, G. A. Covic, and J. T. Boys, "A parallel topology for inductive power transfer power supplies," *IEEE Trans. Power Electron.*, vol. 29, no. 3, pp. 1140–1151, Mar. 2014.

[20] C.-S. Wang, G. A. Covic, and O. H. Stielau, "Power transfer capability and bifurcation phenomena of loosely coupled inductive power transfer systems," *IEEE Trans. Ind. Electron.*, vol. 51, no. 1, pp. 148–157, Feb. 2004.

[21] Z. N. Low, R. A. Chinga, R. Tseng, and J. Lin, "Design and test of a high-power high-efficiency loosely coupled planar wireless power transfer system," *IEEE Trans. Ind. Electron.*, vol. 56, no. 5, pp. 1801–1812, May 2009.

[22] J. Sallan, J. L. Villa, A. Llombart, and J. F. Sanz, "Optimal design of ICPT systems applied to electric vehicle battery charge," *IEEE Trans. Ind. Electron.*, vol. 56, no. 6, pp. 2140–2149, Jun. 2009.

[23] J. U. W. Hsu, A. P. Hu, and A. Swain, "A wireless power pickup based on directional tuning control of magnetic amplifier," *IEEE Trans. Ind. Electron.*, vol. 56, no. 7, pp. 2771–2781, Jul. 2009.

[24] G. Elliott, S. Raabe, G. A. Covic, and J. T. Boys, "Multiphase pickups for large lateral tolerance contactless power-transfer systems," *IEEE Trans. Ind. Electron.*, vol. 57, no. 5, pp. 1590–1598, May 2010.

[25] M. L. G. Kissin, G. A. Covic, and J. T. Boys, "Steady-state flat-pickup loading effects in polyphase inductive power transfer systems," *IEEE Trans. Ind. Electron.*, vol. 58, no. 6, pp. 2274–2282, Jun. 2011.

[26] F. F. A. van der Pijl, M. Castilla, and P. Bauer, "Adaptive sliding-mode control for a multiple-user inductive power transfer system without need for communication," *IEEE Trans. Ind. Electron.*, vol. 60, no. 1, pp. 271–279, Jan. 2013.

[27] S. Chopra and P. Bauer, "Driving range extension of EV with on-road contactless power transfer—A case study," *IEEE Trans. Ind. Electron.*, vol. 60, no. 1, pp. 329–338, Jan. 2013.
[28] D. Kurschner, C. Rathge, and U. Jumar, "Design methodology for high efficient inductive power transfer systems with high coil positioning flexibility," *IEEE Trans. Ind. Electron.*, vol. 60, no. 1, pp. 372–381, Jan. 2013.
[29] J. Shin, S. Shin, Y. Kim, S. Ahn, S. Lee, G. Jung, S.-J. Jeon, and D.-H. Cho, "Design and implementation of shaped magnetic-resonance-based wireless power transfer system for roadway-powered moving electric vehicles," *IEEE Trans. Ind. Electron.*, vol. 61, no. 3, pp. 1179–1192, Mar. 2014.
[30] Ferrox Cube. *Design of planar power transformers.* [Online]. Available: http://www.ferroxcube.com/appl/info/plandesi.pdf
[31] C. T. Rim and G. H. Cho, "Phasor transformation and its application to the DC/AC analyses of frequency/phase controlled series resonant converters (SRC)," *IEEE Trans. Power Electron.*, vol. 5, no. 2, pp. 201–211, Apr. 1990.
[32] W. Y. Lee, J. Huh, S. Y. Choi, X. V. Thai, J. H. Kim, E. A. Al-Ammar, M. A. El-Kady, and C. T. Rim, "Finite-width magnetic mirror models of mono and dual coils for wireless electric vehicles," *IEEE Trans. Power Electron.*, vol. 28, no. 3, pp. 1413–1428, Mar. 2013.
[33] S. Choi, J. Huh, S. Lee, and C. T. Rim, "New cross-segmented power supply rails for roadway powered electric vehicles," *IEEE Trans. Power Electron.*, vol. 28, no. 12, pp. 5832–5841, Dec. 2013.
[34] G. A. Covic and J. T. Boys, "Modern trends in inductive power transfer for transportation applications," *IEEE J. Emerg. Sel. Topics Power Electron.*, vol. 1, no. 1, pp. 28–41, Mar. 2013.
[35] C. B. Park, S. W. Lee, and C. T. Rim, "5m-off-long-distance inductive power transfer system using optimum shaped dipole coils," in *Proc. Int. Power Electron. Motion Control Conf.*, Jun. 2012, pp. 1137–1142.

Changbyung Park (S'10) received the B.S. and M.S degrees in electrical engineering from the Korea Advanced Institute of Science and Technology (KAIST), Daejeon, Korea, in 2008 and 2010, respectively He is currently working toward the Ph.D. degree at KAIST.

He has worked on developing an LED driver IC and a column driver IC for LCD, and wireless power transfer system. His current research interests include wireless power transfer system and touch read-out circuit.

Sungwoo Lee received the B.S. degree from Korea University, Seoul, Korea, in 2007, and the Integrated Master's Ph.D. degree in electrical engineering from the Korea Advanced Institute of Science and Technology (KAIST), Daejeon, Korea.

He has been working at Samsung electronics, Yong-In, Korea. His research interests are in the field of analog integrated circuit design, and his current research interests include the power management IC and in the contactless power supply.

Gyu-Hyeong Cho (S'76–M'80–SM'11) was born in Korea in 1953. He received the B.S. degree from Hanyang University, Seoul, Korea, and the M.S. and Ph.D. degrees in electrical engineering from the Korea Advanced Institute of Science and Technology (KAIST), Daejeon, Korea, in 1975, 1977, and 1981, respectively.

From 1982 to 1983, he was with the Westinghouse R&D Center, Pittsburgh, PA, USA, and joined the Department of Electrical Engineering, KAIST, in 1984. He has been a Tenured Professor since 1991 and was a Visiting Professor at the University of Wisconsin, Madison, in 1989. He performed research in the area of power electronics until the late 1990s and has worked on soft-switching converters, high-power and high-voltage inverters, and static VAR compensators; he later shifted to researching analog integrated circuit designs. His recent research focuses on two areas. One is the combined area of analog integrated circuits and power electronics, including smart power ICs, such as single-chip power management ICs and Class D audio power amplifiers. The other area is display driver ICs for LED, OLED, and LCD flat panel displays.

Chun T. Rim (M'90–SM'11) was born in Korea in 1963. He received the B.S. degree in electrical engineering from the Kumoh National Institute of Technology, Gumi-si, Korea, in 1985, and the M.S. and Ph.D. degrees in electrical engineering from the Korea Advanced Institute of Technology (KAIST), Daejeon, Korea, in 1987 and 1990, respectively.

Since 2007, he has been an Associate Professor of Nuclear and Quantum Engineering, and an adjunct to Aerospace Engineering in Power Electronics at KAIST. He is currently developing inductive power transfer systems for On-Line Electrical Vehicles and leading the Nuclear Power Electronics and Robots Lab, named the *Tesla Lab*, at KAIST. From 1990 to 1995, he was a Military Officer at the Ministry of National Defense in Korea. From 1995 to 2003, he was a Senior Researcher at the Agency for Defense Development, Daejeon, and from 1997 to 1999, he was with Astrium in Portsmouth, U.K. From 2003 to 2007, he was a Senior Director at the Presidential Office, Seoul, Korea. He was involved in developing Korea's first airborne and spaceborne Synthetic Aperture Radars. His research interests include wireless electric vehicles, wireless power systems for robots and bio-medical applications, and energy grid applications. He has authored or coauthored 81 technical papers, written four books, and holds more than 99 patents (awarded and pending).

Dr. Rim has received three prizes from the Korean government.